Chinese Chemical Letters 35 (2024) 109120

Contents lists available at ScienceDirect

Chinese Chemical Letters

journal homepage: www.elsevier.com/locate/cclet

Construction of metal-organic frameworks with unsaturated Cu sites for efficient and fast reduction of nitroaromatics: A combined experimental and theoretical study

Longlong Geng[a,b], Huiling Liu[a], Wenfeng Zhou[a,b], Yong-Zheng Zhang[a,*], Hongliang Huang[c], Da-Shuai Zhang[a,b,*], Hui Hu[a], Chao Lv[a], Xiuling Zhang[a,b], Suijun Liu[d,*]

[a] Shandong Provincial Key Laboratory of Monocrystalline Silicon Semiconductor Materials and Technology, College of Chemistry and Chemical Engineering, Dezhou University, Dezhou 253023, China
[b] School of Chemistry and Chemical Engineering, Shandong University of Technology, Zibo 255000, China
[c] State Key Laboratory of Separation Membranes and Membrane Processes, School of Chemical Engineering and Technology, Tiangong University, Tianjin 300387, China
[d] School of Chemistry and Chemical Engineering, Jiangxi Provincial Key Laboratory of Functional Molecular Materials Chemistry, Jiangxi University of Science and Technology, Ganzhou 341000, China

ARTICLE INFO

Article history:
Received 8 August 2023
Revised 6 September 2023
Accepted 18 September 2023
Available online 20 September 2023

Keywords:
Metal-organic frameworks
Open metal sites
Catalysis
Copper node
4-Nitrophenol

ABSTRACT

Metal-organic frameworks (MOFs) functionalized with open metal sites (OMSs) have received widespread attention in various applications due to their fascinating electronic properties and unique interactions with guest molecules. However, rational tailoring of the coordination environment of metal nodes during the synthesis of MOFs remains a great challenge due to their tendency of saturated coordination with linkers. Herein, we reported the construction of three new MOFs featuring unsaturated Cu(II) sites, namely $[Cu(HCOO)(pzta)]_n$ (**HL-1**), $\{[Cu(PTA)_{0.5}(pzta)(H_2O)]\cdot 2H_2O\}_n$ (**HL-2**) and $[Cu(NA)_{0.5}(pzta)]_n$ (**HL-3**) (Hpzta = 3-pyrazinyl-1,2,4-triazole; PTA = terephthalic acid; NA = 1,4-naphthalene dicarboxylic acid), based on the mixed-linker strategy *via* specific selection of versatile Hpzta ligand and carboxylate ligands. Remarkably, the obtained MOFs exhibited excellent activity and good recyclability for the catalytic reduction of nitroaromatics under mild conditions (25 °C and 1 atm). In particular, the complete conversion of 4-nitrophenol (4-NP) took only 30 s on **HL-2**, reaching a record-high TOF value compared with previously reported metal catalysts. The combined experimental and theoretical studies on **HL-2** revealed that the open Cu site with positive-charged nature could improve the adsorption and subsequent electron transport between the substrates, and was responsible for the outstanding performance. This work shined lights on the further enhancement of performance for MOFs through rational OMSs construction.

Metal-organic frameworks (MOFs), which are built from metal ions/clusters linked together by organic ligands, have been considered as multifunctional platforms due to their modular structure, intriguing porosity as well as adjustability in physiochemical properties [1–4]. In particular, MOFs with open metal sites (OMSs) received extensive attention in recent years, and are regarded as promising candidates for advanced materials since its first confirmation by Omar M. Yaghi *et al.* in 2000 [5–8]. In general, the metal nodes tend to be coordinatively saturated with functional linkers based on principles of reticular synthesis. Hence, the formation of OMSs in MOFs could not only optimize the pore structure of the framework but also modulate the electron density of the metal nodes, which in return trigger unusual interactions between the guest molecules and metal sites [8–10]. Till now, extensive computational and experimental studies have confirmed that OMSs play a performance-determining role in the applications in MOFs, such as gas sorption and separation, catalysis, sensing [11–19]. For example, OMSs functionalized MOFs are among the most promising adsorbents with ultrahigh H_2 uptake [11], exceptional selectivity in CO_2 removal from gas mixtures [12], and have been described as highly active catalysts for organic transformations, including selective oxidation of alcohols [13], reduction of unsaturated imines [14], CO_2 cycloaddition to synthesize epoxides [15], photo-fenton degradation of acetamiprid [17], as well as the cyclization of citronellal to isopulegols [19].

* Corresponding authors.
E-mail addresses: zhangyongzheng23@163.com (Y.-Z. Zhang), dashuai_74@163.com (D.-S. Zhang), sjliu@jxust.edu.cn (S. Liu).

https://doi.org/10.1016/j.cclet.2023.109120
1001-8417/

It should be noted that, although there is a myriad of successful applications that have benefited from the utilization of OMSs-containing MOFs, the balance between further enhancement of performance and the concentration of OMSs as well as structural stability of the MOFs remains an open question. Since the top-down removal of ligands and/or solvent molecules *via* an activation strategy is currently a prerequisite for the construction of OMSs in MOFs [20–22], which can be further extended to thermal, chemical, or photothermal activation. In many instances, unfortunately, complex and extremely precise regulations on activation conditions are required to minimize the potential structural transformation or even complete decomposition. Recently, R. A. Fischer *et al.* and M. Oh's group achieved the synthesis of HKUST-1 and MOF-74 with structural defects *via* partial replacement of the organic linkers by defective linkers [23,24]. They found that implementing defects into the framework can contribute OMSs for catalytic applications. However, the distribution and concentration of OMSs are somewhat low in most MOFs [25–27]. Therefore, expanding and exploring new strategy for OMSs construction remains a challenge but crucial to fully exploit their potential on a larger scale.

For crystalline materials, the microstructure design and regulation through rational modification of synthetic factors, such as type of metal/ligand, ratio, oxidation state, or fabrication environment, is the most fundamental approach [28–30]. And one field that has especially benefited from this discipline is the construction of MOFs as advanced materials. Notably, some success has been achieved in aligning the geometry, size topology, and coordination mode of MOFs by rational selection of the ligands with unique functional groups (*e.g.*, pyridine or pyrazole groups) and/or spatial configurations (such as asymmetric chelate sites) [31–37]. These preliminary works give us fascinating inspiration and motivation to explore efficient strategy for the construction of OMSs in MOFs.

Herein, we reported the assembly of 3-pyrazinyl-1,2,4-triazole (Hpzta) ligand with Cu(II) ions ensure the formation of second building unit (SBU, $Cu_2(pzta)_2$) with unsaturated Cu sites in **HL-1**. In view of configuration tailoring, another two new MOFs (**HL-2** and **HL-3**) with different configuration were constructed through a mixed-linker strategy. In these MOFs, the $Cu_2(pzta)_2$ SBUs were linked by diverse second carboxylate ligands (PTA for **HL-2**, and NA for **HL-3**) to form the framework with different dimensions. The single-crystal X-ray diffraction results revealed that the unsaturated Cu sites in **HL-1** and **HL-3** were blocked by the adjacent $Cu_2(pzta)_2$ SBUs with a distance about 3–5 Å, respectively, while in **HL-2** it was unobstructed. Their catalytic activity, reaction kinetics and thermodynamic characteristics in the reduction of nitroaromatics are investigated systematically. Furthermore, the correlation between the catalytic activity and the coordination structure and electronic properties of open copper sites was also explored by a combined experimental and theoretical study, and finally a possible reduction mechanism is also hypothesized.

The solvothermal reactions between mixed-ligands (Hpzta and carboxylate ligand) and Cu(II) salt in solution of DMF/DMA and water yielded the crystals of **HL-1**, **HL-2**, and **HL-3**, respectively (Fig. 1, more synthesis details see Experimental Section in Supporting information). Based on the single-crystal X-ray diffraction analysis, each Cu(II) ion is five-coordinated by three N atoms from two Hpzta ligands and two O atoms from *in-situ* formed formate ligand/water molecules, forming a slightly distorted CuN_3O_2 square-pyramid geometry (Figs. 1a–c). For **HL-1**, two adjacent Cu(II) ions were bonded together by two Hpzta ligands to generate $Cu_2(pzta)_2$ SBU with two unsaturated Cu sites, where Cu(II) ions and coordinated N atoms took in a plane (more crystal parameters see Table S1 in Supporting information). Furthermore, the $Cu_2(pzta)_2$ SBUs connected by formate in a μ_2-η^1:η^1 mode to form a two-dimensional (2D) network (Fig. 1d), and these 2D networks packed

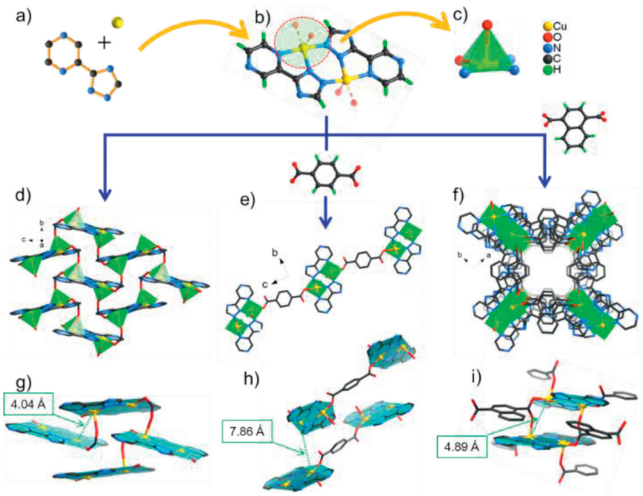

Fig. 1. (a, b) Assembly of Hpzta with Cu ions into $Cu_2(pzta)_2$ SBU and (c) configuration of coordination mode for Cu atom. (d) 2D layer network of **HL-1**, (e) 1D band of **HL-2** and (f) 3D framework of **HL-3**. Packing mode and minimum Cu-Cu distance of the adjacent $Cu_2(pzta)_2$ SBUs in (g) **HL-1**, (h) **HL-2** and (i) **HL-3** (selected hydrogen atoms are omitted for clarity).

in an AA stacking mode *via* intermolecular hydrogen bonding (Fig. S1a and b in Supporting information).

It should be noted that the formic acid in **HL-1** is *in-situ* formed by the decomposition of DMF solvent. Based on the mind that the formate linker might be replaced by other carboxylate ligands, consequently, dicarboxylic acid was further incorporated as bridging ligands during MOFs synthesis to adjust the openness of the unsaturated Cu sites in $Cu_2(pzta)_2$ SBUs. As shown in Fig. 1e, the PTA ligand linked the $Cu_2(pzta)_2$ SBUs to yield a 1D chain running along *c* axis (**HL-2**). The slight coordination difference from **HL-1** is that, in **HL-2**, the coordinated oxygen atom in the vertex of the CuN_3O_2 square-pyramid is water molecule rather than carboxyl oxygen atom. There were also two free water molecules in the asymmetric unit of **HL-2**. Additionally, hydrogen bond interactions were formed not only between water molecules, but also between water molecules and 1D chains, giving the 3D supramolecular structure of **HL-2** (Figs. S1c and d in Supporting information).

When NA was used as the bridging ligand for $Cu_2(pzta)_2$ unit, a 3D framework (**HL-3**) was constructed, which possesses the narrow 1D square channels (<4.1 Å) along *c* axis (Fig. 1f). In **HL-3**, different from **HL-2**, carboxylate connected Cu(II) ion in a μ_2-η^1:η^1 mode, each NA bridged four SBUs and each $Cu_2(pzta)_2$ SBU linked to four NA (Fig. S1e in Supporting information). Topologically, the 3D framework of **HL-3** can thus be regarded as a (4,4)-connected network with the point symbol of (4^2) (8^4) (Fig. S1f in Supporting information). As shown in Figs. 1g-i, the Cu sites were blocked by the adjacent $Cu_2(pzta)_2$ SBUs in **HL-1** and **HL-3** with a close distance about 3–5 Å and a minimum Cu-Cu distance of 4.04 Å and 4.89 Å, respectively. For **HL-2**, however, the adjacent SBUs were arranged at a spatial interval with a minimum Cu-Cu distance of 7.86 Å (Fig. 1h), this value is obviously higher than those of **HL-1** and **HL-3**. Therefore, it is reasonable to assume that the Cu sites in three MOFs may present different accessibility to the external environment during catalysis process owing to the modulated skeleton arrangement.

The textural parameters of the Cu-MOFs characterized by N_2 adsorption are shown in Fig. S2 and Table S2 (Supporting information). The calculated surface area (S_{BET}) and pore volume centered at 12–22 m^2/g and 0.09–0.14 cm^3/g, respectively. The crystalline structure and thermal stability of the synthesized MOFs were investigated by powder X-ray diffraction (XRD) and thermogravimet-

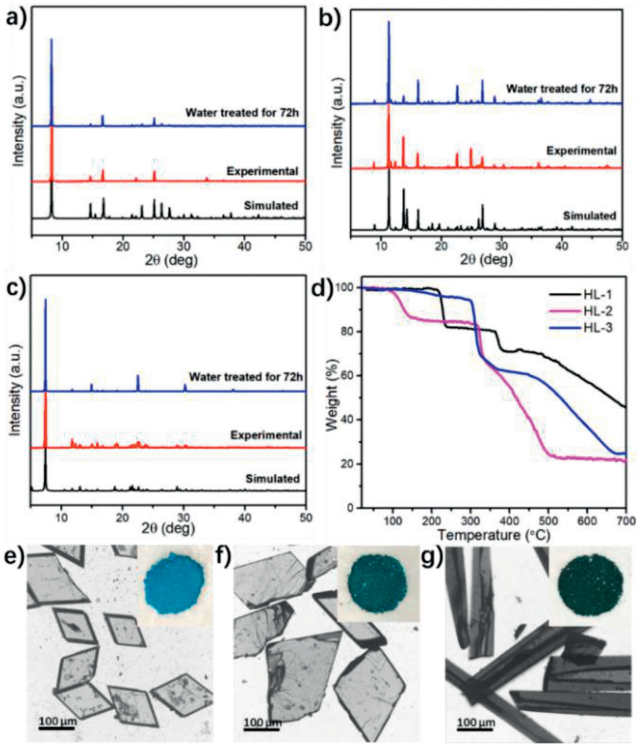

Fig. 2. XRD patterns of the synthesized (a) **HL-1**, (b) **HL-2**, (c) **HL-3**. (d) TGA curves of the MOFs, and microscopy images of (e) **HL-1**, (f) **HL-2**, (g) **HL-3**.

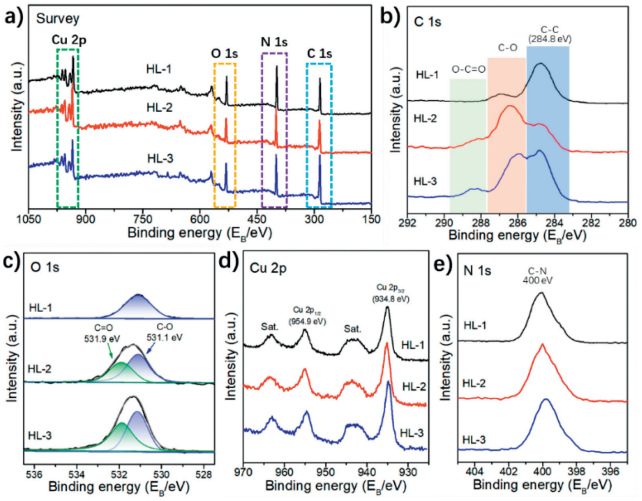

Fig. 3. (a) XPS survey spectra and fine spectra of (b) C 1s, (c) O 1s, (d) Cu 2p and (e) N 1s of the obtained MOFs.

ric analysis (TGA). As depicted in Figs. 2a–c, the XRD spectra of all three MOFs show strong Bragg diffraction peaks and match the main peaks of the simulated spectra, indicating their good crystallinity and high purity. Besides, the main character peaks in XRD patterns still maintained after immersing the solids in water for 72 h, confirming their relatively high stability, which are attractive virtues for their catalytic applications. TGA curves in Fig. 2d reveal that **HL-1** and **HL-3** are stable in N_2 atmosphere up to 240 °C and 320 °C, respectively. As for **HL-2**, the TGA curve experienced two major weightlessness at 110–150 °C and 325–500 °C. According to its crystal structure, the former mainly originated from the removal of the free H_2O molecules, and the latter is mainly caused by the decomposition of the framework. The optical photographs further confirmed the morphology and structure of the as-synthesized MOFs. As shown in the insets of Figs. 2e-g, all MOFs are presented as solid powders, colored blue for **HL-1**, green for **HL-2**, and dark green for **HL-3**, respectively. It can be seen in the enlarged microscopy images that both **HL-1** and **HL-2** assembled into a two-dimensional sheet-shaped structure along the horizontal but a diamond and irregular morphology in the vertical direction. The size of the MOF nanosheets centered at 500–2000 nm. As for **HL-3**, a one-dimensional rod-like morphology was observed with a diameter of 50–100 μm and a length of 1000 μm.

To define the chemical composition and valence of elements in the as-synthesized MOFs, the XPS spectrum was further recorded. XPS survey spectra in Fig. 3a show that the obtained MOFs are composed of elements C, N, O, and Cu, indicating their similar surface chemical composition. Fig. 3b displayed the C 1s XPS spectra of the MOFs, and three types of carbon atoms could be assigned according to the literature, including C=C bonds at 284.8 eV, C–O bonds in the range of 285.5–287.4 eV and C=O and/or O–C=O species at a higher bonding energy of 288.6 eV [38,39]. Compared with **HL-1**, an obvious increase in the peak intensity of C–O and C=O species was confirmed for **HL-2** and **HL-3**, which should be originated from the carboxylate ligands in their frameworks. This hypothesis was further confirmed by the O 1s XPS results. As demonstrated by Fig. 3c, the O 1s peak could be fitted into two kinds of oxygen species: Ether groups (531.1 eV) and carbonyl groups (531.9 eV) [40]. It is obviously that higher content of carbonyl groups was detected in **HL-2** and **HL-3** than those in **HL-1**. The high-resolution Cu 2p XPS spectrum is given in Fig. 3d. The Cu $2p_{3/2}$ and Cu $2p_{1/2}$ core level around the bonding energy of 934.8 eV and 954.9 eV could be identified in the spectrum of **HL-1**, **HL-2**, and **HL-3**, indicating a similar chemical environment of Cu species. Besides, the two additional satellite peaks at 943.3 eV and 963.3 eV further reveal the valence state of Cu species is +2 [41,42]. Notably, compared with that of CuO (933.8 eV and 953.6 eV), the Cu 2p peaks for MOFs shifted towards higher binding energy, indicating a positively charged nature of the Cu sites, which should be closely related to its carboxylic acid coordinated microstructure according to the single crystal results. In addition, due to the usage of the same N-containing ligand for all samples, similar N 1s XPS spectra were obtained (Fig. 3e). The direct coordination of Cu with N atoms is an advantage of the newly synthesized MOFs for their catalytic applications, since the strong electron injection ability of the N species has been proved to be conducive to promoting the charge transfer ability of the coordinated metal species, thus achieving improved catalytic performance [38].

The open metal sites, positively-charged Cu nodes, and high stability confirm the obtained MOFs ideal candidates for catalytic applications. Therefore, their catalytic performance was further evaluated in the catalytic transformation of 4-nitrophenol (4-NP) to synthesize 4-aminophenol (4-AP) through a reduction route. The title reaction has a significant prospect for industrial application and has been extensively applied as a model reaction in literatures [43–45]. In view of green chemistry and energy conservation, in this study, the reaction was carried out at atmospheric temperature and pressure (25 °C, 1 atm) using H_2O and $NaBH_4$ as the solvent and reductive agent. Fig. 4 summarized the catalytic performance of 4-NP reduction over the as-synthesized MOFs. The result of the blank experiment reveals that the reduction of 4-NP does not occur without the addition of any catalyst. Over CuO catalyst, a 54.3% conversion of 4-NP was obtained in 6 min reaction. Compared with CuO, we can see from Fig. 4a that all the Cu-based MOFs showed significantly improved reduction performance. For example, the reaction time for the complete reduction of 4-NP decreased to 3 min for **HL-3** and 1.5 min for **HL-1**, respectively. Remarkably, over **HL-2**, the complete conversion of 4-NP was achieved only

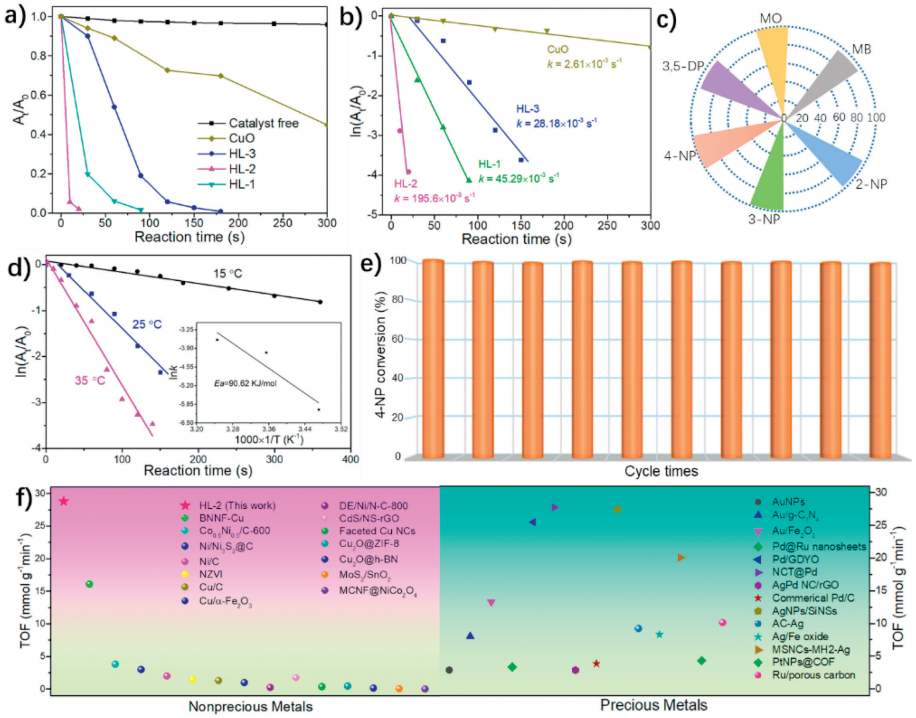

Fig. 4. Catalytic performance of nitroaromatics reduction: Plot of (a) A_t/A_0 *vs.* reaction time and (b) $\ln(A_t/A_0)$ *vs.* reaction time for 4-NP reduction in the presence of the Cu-based catalysts. (c) Conversion of different substrates catalyzed by **HL-2**. (d) Plot of $\ln(A_t/A_0)$ *vs.* reaction time for 4-NP reduction on **HL-2** at different temperature. (e) Recycle capability test of **HL-2** for the reduction of 4-NP. (f) Comparison of the performance of 4-NP reduction over recently reported metal-based catalysts.

in 30 s, exhibiting superior catalytic performance under the same conditions.

Similar to previous reports, an excess amount of $NaBH_4$ to 4-NP was used in this work. Hence, a pseudo-first-order kinetic model was applied for the kinetic study and calculation of the apparent rate constant (k) [44,45]. As illustrated in Fig. 4b, the calculated k for 4-NP reduction is 195.6×10^{-3} s^{-1} for **HL-2**, which is about 75-fold higher than that of CuO and even higher than that of the homogeneous Cu catalysts (Table S3 in Supporting information). The rate constant (k) met the trend: **HL-2** (195.6×10^{-3} s^{-1}) > **HL-1** (45.3×10^{-3} s^{-1}) > **HL-3** (28.2×10^{-3} s^{-1}) > CuO (2.6×10^{-3} s^{-1}). Apart from 4-NP, catalytic reduction of other nitrophenols and organic dye molecules over **HL-2** was also investigated and the results were displayed in Fig. 4c. It shows that **HL-2** could effectively catalyze the reduction of 2-nitrophenol (2-NP), 3-nitrophenol (3-NP), 3,5-dinitrophenol (3,5-DP), methyl orange (MO) and methylene blue (MB) with ≥95% conversion under mild conditions. Additionally, as demonstrated by Fig. 4d, the rate constant (k) gradually increased with increasing the reaction temperature, implying that the reduction of 4-NP is thermodynamically favorable over **HL-2**. Furthermore, the activation energy (E_a) was investigated using the classical Arrhenius equation. The inset in Fig. 4d depicted the plot of ln$k$ *versus* 1/T. Based on the linear fits, the E_a was calculated to be 90.62 kJ/mol for **HL-2**.

Apart from the catalytic activity, the durability and reusability of the catalyst are also key parameters for their practical applications. Fig. 4e depicted the consecutive cycle test of **HL-2** for 4-NP reduction. Impressively, **HL-2** could be consecutively used at least 10 times without observable degradation in efficiency, which should be associated with its high stability. XRD pattern of the reused **HL-2** revealed no significant change in the crystallinity in comparison to the fresh sample (Fig. S3 in Supporting information), confirming its usage potential for practical catalysis. Thus, a large-scale reduction of 4-NP was carried out. The amplification test in Fig. S4 (Supporting information) confirmed that **HL-2** is still highly active with the increase of 4-NP dosage (scale-up 8-fold, 18-fold and 36-fold, for example), and achieved a maximum turnover frequency (TOF) of 28.8 mmol g^{-1} min^{-1} under ambient conditions. Fig. 4f and Table S3 briefly summarized the catalytic activities of **HL-2** as well as some recently reported catalysts. Impressively, **HL-2** displayed a record high TOF compared to most literature-reported non-noble metal catalysts and certain precious-metal-containing catalysts, confirming its potential application prospects in the field of nitroaromatics reduction.

For the reduction mechanism studies of 4-NP, Esumi and collaborators demonstrated previously that the transformation involves two rate-determining steps: (1) The adsorption of 4-NP on the active sites (through either physical absorption or electrostatic interaction) and (2) the efficient electron transfer from the hydrogen donor to the acceptor 4-NP mediated by the catalyst [46]. Oyama *et al.* also highlighted that the activity of 4-NP reduction is strongly influenced by the coordination and electronic structure of metal sites, which determines the adsorption and activation of reactants on the catalyst [47]. For **HL-2** in this study, the superior performance in 4-NP reduction should be correlated to the synergy effects of the unique spatial configuration of the framework and richness of open Cu sites. To gain a deeper understanding of the positive effect of open Cu sits on 4-NP activation and illustrate the mechanism of the 4-NP reduction over **HL-2**, DFT calculations were further conducted. All computations were done on the model system according to the crystallographic data. First of all, the adsorption properties of 4-NP over **HL-2** were studied and the plausible adsorption configurations and the adsorption energies are summarized in Fig. 5a and Fig. S5 (Supporting information). Based on our calculations and the previous related study [43], the most stable configuration of 4-NP over **HL-2** was set to be parallel to the catalyst surface.

Fig. 5b depicted the DFT-calculated potential energy profile and the corresponding configurations for the reduction pathway of 4-NP to 4-AP catalyzed by the open Cu sites over **HL-2**. The reduc-

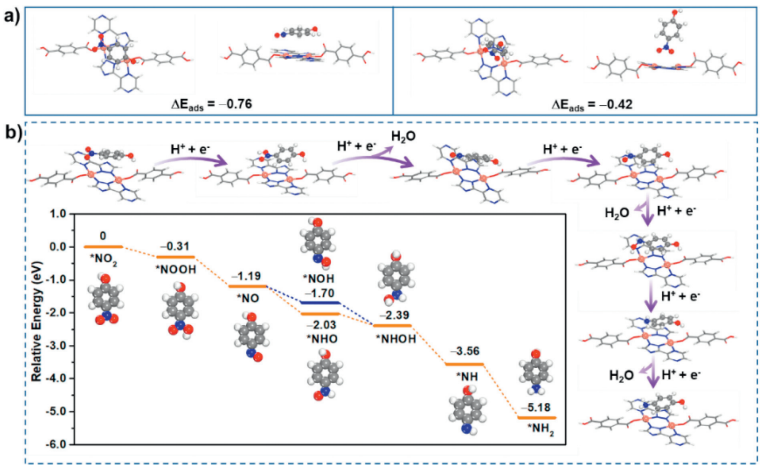

Fig. 5. (a) Plausible optimized configurations of 4-NP adsorbed on **HL-2**. (b) Schematic diagram of the reaction pathway for the reduction of 4-NP to 4-AP over **HL-2**. The inset shows the potential energy diagram of 4-NP reduction. The outer circle displays the corresponding calculated intermediates.

tion reaction was first triggered by the adsorption of 4-NP with an adsorption energy of −0.76 eV. The first protonation step occurs with the oxygen atom of 4-NP combining with a hydrogen atom to form a *NOOH intermediate, which is exothermic step of −0.31 eV. Subsequently, the *NOOH intermediate is dehydroxylated to *NO with releasing a H_2O molecule ($\Delta E = -0.88$ eV). The formed *NO is further hydrogenated into *NHO with a large energy release of −0.88 eV, while the conversion of *NO-to-*NOH step is less feasible with a smaller reaction energy of −0.51 eV. On the formation of *NHO, the hydrogenation step leading to the *NHOH formation is thermodynamically relevant with the reaction potential energies of −0.36 eV. The formed *NHOH is then further dehydrated into the *NH intermediate with the exergonicity of −1.17 eV before the formation of the final product of 4-AP ($E = -1.62$ eV) by the third hydrogenation. The complete hydrogenation reduction of 4-NP to 4-AP over **HL-2** catalyst follows the reaction pathway $*NO_2$ (4-NP) → *NOOH → *NO → *NHO → *NHOH → *NH → $*NH_2$ (4-AP).

Via a combined analysis of both experimental and theoretical results, the pivotal role of open Cu sites in **HL-2** for the efficient and fast reduction of nitroaromatics could be ascribed as follows: The unique spatial configuration endow the surface Cu sites with higher accessibility in the framework, which improves the contact of substrates during reaction. Secondly, the positively-charged nature of the open Cu sites can further enhance the adsorption and activation of negatively charged 4-NP molecules, which is essential for subsequent reduction steps. Moreover, the electron-rich N species coordinated with Cu species could improve the charge transport capacity of the catalyst and make it easier for the reduction of 4-NP to occur on the Cu sites.

In summary, three new Cu-based MOFs were hydrothermally synthesized and characterized clearly, and exhibited outstanding catalytic performance for reducing 4-NP under atmospheric conditions. The complete conversion of 4-NP took only 30 s over **HL-2**, giving a record-high k value of 195.6×10^{-3} s^{-1} and TOF value of 28.8 mmol g^{-1} min^{-1}. Combined structural analysis and DFT calculations uncovered the open and accessible Cu site with positive-charged character was responsible for the excellent catalytic performance, which improves the adsorption and subsequent electron transport between the substrates. In addition, **HL-2** could be reused at least ten times without fading in activity, exhibiting the usage potential for practical application. This work underlines the importance of ligands for OMSs design during MOF synthesis, which may be a promising direction for the construction of novel OMSs functionalized MOFs with multifunctional performance.

Declaration of competing interest

The authors declare that we have no known competing financial interests or personal relationships that could have appeared to influence the work reported in this paper.

Acknowledgments

This work was supported by the National Natural Science Foundation of China (Nos. 21902022, 81903501 and 21601028), Qingchuang Science and Technology Plan of Shandong Province (No. 2021KJ054), the Natural Science Foundation of Shandong Province (Nos. ZR2018LB018, ZR2019QB026, ZR2022QB058 and ZR2020KB014) and Scientific Research Foundation of Dezhou University (Nos. 30101905, 30102708, 30102701).

Supplementary materials

Supplementary material associated with this article can be found, in the online version, at doi:10.1016/j.cclet.2023.109120.

References

[1] H. Furukawa, K.E. Cordova, M. O'Keeffe, O.M. Yaghi, Science 341 (2013) 1230444.
[2] B. An, Z. Li, Y. Song, et al., Nat. Catal. 2 (2019) 709–717.
[3] D. Wang, M. Suo, S. Lai, et al., Appl. Catal. B: Environ. 321 (2023) 122054.
[4] C. Dong, J.J. Yang, L.H. Xie, et al., Nat. Commun. 13 (2022) 4991.
[5] B. Chen, M. Eddaoudi, T.M. Reineke, et al., J. Am. Chem. Soc. 122 (2000) 11559–11560.
[6] F. Zhang, J. Zhang, B. Zhang, et al., Nat. Commun. 11 (2020) 1431.
[7] Ü. Kökçam-Demir, A. Goldman, L. Esrafili, et al., Chem. Soc. Rev. 49 (2020) 2751–2798.
[8] J. Sun, X. Zhang, D. Zhang, et al., CCS Chem. 4 (2022) 996–1006.
[9] A. Liu, X. Peng, Q. Jin, et al., ACS Appl. Mater. Interfaces 11 (2019) 4686–4700.
[10] G. Si, X. Kong, T. He, et al., Chin. Chem. Lett. 32 (2021) 918–922.
[11] D.J. Levine, T. Runčevski, M.T. Kapelewski, et al., J. Am. Chem. Soc. 138 (2016) 10143–10150.
[12] R. Poloni, B. Smit, J.B. Neaton, J. Am. Chem. Soc. 134 (2012) 6714–6719.
[13] Q.Q. Huang, Z.B. Fang, K. Pang, et al., Adv. Funct. Mater. 32 (2022) 2205147.
[14] Z. Niu, W. Zhang, P.C. Lan, B. Aguila, S. Ma, Angew. Chem. Int. Ed. 58 (2019) 7420–7424.
[15] G. Cai, X. Ma, M. Kassymova, et al., ACS Cent. Sci. 7 (2021) 1434–1440.
[16] Q.Y. Zhu, L.P. Zhou, Q.F. Sun, Dalton Trans. 48 (2019) 4479–4483.
[17] Y. Wang, Z. Zhong, Y. Muhammad, et al., Chem. Eng. J. 398 (2020) 125684.
[18] N. Rezvani Jalal, T. Madrakian, A. Afkhami, A. Ghoorchian, ACS Appl. Mater. Interfaces 12 (2020) 4859–4869.
[19] J.N. Hall, P. Bollini, React. Chem. Eng. 4 (2019) 207–222.
[20] X.J. Kong, J.R. Li, Engineering 7 (2021) 1115–1139.
[21] L. Jiao, J. Wang, H.L. Jiang, Acc. Mater. Res. 2 (2021) 327–339.
[22] H.X. Zhang, Q.L. Hong, J. Li, et al., Angew. Chem. Int. Ed. 58 (2019) 11752–11756.

[23] Z. Fang, J.P. Dürholt, M. Kauer, et al., J. Am. Chem. Soc. 136 (2014) 9627–9636.
[24] H. Jun, S. Oh, G. Lee, M. Oh, Sci. Rep. 12 (2022) 14735.
[25] Z.W. Zhang, H. Hu, M.Z. Wang, et al., CrystEngComm 24 (2022) 8509–8516.
[26] X. Zhang, Y.Z. Zhang, Y.Q. Jin, et al., Inorg. Chem. 59 (2020) 11728–11735.
[27] X. Zhang, Y. Zhang, W. Zhou, et al., Chin. Chem. Lett. 34 (2023) 107368.
[28] Z. Chen, P. Li, R. Anderson, et al., Science 368 (2020) 297–303.
[29] F. Wang, Z.S. Liu, H. Yang, Y.X. Tan, J. Zhang, Angew. Chem. Int. Ed. 50 (2011) 450–453.
[30] G.P. Yang, K. Li, C.W. Hu, Inorg. Chem. Front. 9 (2022) 5408–5433.
[31] J. Hwang, A. Ejsmont, R. Freund, et al., Chem. Soc. Rev. 49 (2020) 3348–3422.
[32] X. Zheng, S. Qi, Y. Cao, et al., Chin. J. Catal. 42 (2021) 279–287.
[33] L. Wu, S. Yao, H. Xu, et al., Chin. Chem. Lett. 33 (2022) 541–546.
[34] X.H. Yi, Y. Gao, C.C. Wang, et al., Chin. Chem. Lett. 34 (2023) 108029.
[35] W. Yan, X. Cao, R. Wang, et al., J. Solid State Chem. 275 (2019) 167–173.
[36] L. Yang, P. Cai, L. Zhang, et al., J. Am. Chem. Soc. 143 (2021) 12129–12137.
[37] J. Ren, Y. Huang, H. Zhu, et al., Carbon Energy 2 (2020) 176–202.
[38] X. Zhang, N. Wang, L. Geng, et al., J. Colloid Interface Sci. 512 (2018) 844–852.
[39] Y. Zhu, W.D. Wang, X. Sun, et al., ACS Appl. Mater. Interfaces 12 (2020) 7285–7294.
[40] L. Geng, M. Zhang, W. Zhang, et al., Catal. Sci. Technol. 5 (2015) 3097–3102.
[41] L. Geng, G. Li, X. Zhang, et al., J. Solid State Chem. 296 (2021) 121960.
[42] L. Geng, S. An, X. Wang, et al., J. Environ. Chem. Eng. 10 (2022) 108689.
[43] J. Liang, Q. Song, J. Wu, et al., ACS Nano 16 (2022) 4152–4161.
[44] W. Liu, L.M. Ning, S.Q. Li, et al., J. Alloys Compd. 862 (2021) 158333.
[45] K. Rajendran, N. Pandurangan, C.P. Vinod, et al., Appl. Catal. B: Environ. 297 (2021) 120417.
[46] K. Hayakawa, T. Yoshimura, K. Esumi, Langmuir 19 (2003) 5517–5521.
[47] X. Chen, Z. Cai, X. Chen, M. Oyama, J. Mater. Chem. A 2 (2014) 5668–5674.